JOURNAL OF THERMOPHYSICS AND HEAT TRANSFER
Vol. 23, No. 1, January–March 2009

Flow Structures in a U-Shaped Channel

You Qin Wang,* Peter L. Jackson,† and Timothy J. Phaneuf‡
University of Northern British Columbia, Prince George, British Columbia V2N 4Z9, Canada

DOI: 10.2514/1.35147

Numerical investigation of flow through a U-shaped channel with a square cross section is presented in this paper. The primary aim of this study is to determine if FLUENT, a commercial computational fluid dynamics software package, is capable of providing a reasonable solution for this kind of flow configuration. Calculations were performed at Reynolds numbers of 109, 382, and 873 using large-eddy simulation. Simulation results indicate that the present study has successfully reproduced the primary flow as well as most of the flow features associated with the secondary flow. The existence of Dean vortices was consistent with previous experimental studies.

Nomenclature

AR	=	aspect ratio of the rectangle
C_s	=	Smagorinsky constant
c	=	distance between the divider-wall tip and the end wall, m
D	=	length of the side of the square channel, m
d	=	distance to the closest wall, m
G	=	filter function
L_s	=	mixing length for subgrid scales, m
n	=	local x coordinate at the U-bend, m
P	=	pressure, N/m^2
Q_{EAS}	=	normalized measure of skewness
Re	=	Reynolds number
S_{ij}	=	strain rate tensor, $1/s$
t	=	physical time step, s
t^*	=	nondimensional time step
U	=	time-averaged streamwise velocity, m/s
u_i	=	x_i component of velocity, m/s
u_*	=	friction velocity, m/s
V	=	volume of a computational cell, m^3
x	=	streamwise coordinate, m
x_i	=	Cartesian coordinate, m
y	=	spanwise coordinate, m
z	=	vertical coordinate, m
Δy	=	distance from the wall to the first grid point, m
Δy^+	=	first node's wall unit, $\Delta y u_*/\nu$
κ	=	von Kármán constant
μ	=	dynamic viscosity, kg/m/s
μ_t	=	eddy viscosity, kg/m/s
ν	=	kinematic viscosity, m^2/s
ρ	=	fluid density, kg/m^3
τ_{ij}	=	subgrid-scale stress tensor, $kg/m/s^2$

Subscripts

rms	=	root mean square
∞	=	inlet

Received 15 October 2007; revision received 28 April 2008; accepted for publication 4 June 2008.

*Senior Lab Instructor, High Performance Computing Project, College of Science and Management.

†Professor, Environmental Science Program, College of Science and Management.

‡Graduate Student, Environmental Science Program, College of Science and Management.

Introduction

FLOW in serpentine channels is encountered in a number of engineering systems, particularly in chemical processing and heat exchangers. For example, internal blade cooling is employed in modern gas turbines because turbine inlet temperatures have continued to rise over the past several years. This internal cooling involves forced convection inside the blades by means of a serpentine flow passage. Convection can be increased by inducing turbulence in the flow, but at the same time, that also results in an increase of friction in the duct. The ultimate aim behind designing these flow passages is to obtain effective overall cooling of the components at the least penalty on the friction coefficient. Therefore, the efficient design of these internal cooling passages in gas turbine blades requires a detailed knowledge of the flow and heat transfer phenomena. Another example of flow in a serpentine channel is in a proton-exchange-membrane fuel cell. In this system, the membrane–electrode assembly, in which the electrochemical reaction and transport processes take place, is typically sandwiched between two bipolar plates. These bipolar plates, which serve to collect the electric current and supply the reactants through the embedded flow channels, contain serpentine channels. Furthermore, these serpentine channels usually more closely resemble a squared U-bend than a curved channel. Flow in a U-bend channel with a 180 deg sharp turn is characterized by complicated flow structures such as impingement, recirculation, and flow separation and has been the subject of numerous experimental and computational studies. Previous studies examined flow in a two-pass square channel with a sharp 180 deg turn [1–6], a two-pass rectangular channel with a sharp 180 deg turn [7–10], and a serpentine passage with a series of right-angle turns [11–14].

Among computational studies, the most recent numerical simulations were made using in-house codes at a Reynolds number of 20,000 with large-eddy simulation (LES) [15] and detached-eddy simulation (DES) approaches [16]. Both papers presented the flow structure in a 180 deg bend with a square section. Sewall and Tafti [15] compared two configurations in their study: one without a rib in the bend and the other with a rib included in the bend. Both cases showed a pair of counter-rotating Dean vortices in the midplane of the bend, whereas only the case without a rib in the bend showed a large recirculation zone at the tip of the dividing wall. Viswanathan and Tafti [16] studied the case with ribs in two passes by DES and the unsteady Reynolds-averaged Navier–Stokes (URANS) with a base k-ω model and compared their results with LES simulations by Sewall and Tafti [15]. They found that DES does not predict shear-layer transition with accuracy and predicts a greater development length than does LES. However, once the flow is fully developed, DES predictions compare very well with LES and the experiments. URANS, on the other hand, underpredicts the centerline velocities in the developing region. Comparisons with experiments show that DES captures the detailed flow characteristics but URANS does not.

In previous work that considered turbulent flow and heat transfer within rotating U-shaped passages, Su et al. [10] presented detailed

results of mean velocity, mean temperature, and Nusselt number for two Reynolds numbers ($Re = 10,000$ and 100,000) for three different aspect-ratio ducts (AR = 1:1, 1:2, and 1:4). They found that for nonrotating ducts, a pair of symmetric counter-rotating vortices was generated in the bend region for all three different aspect-ratio ducts. But the highest heat transfer enhancement was observed in the AR = 1:2 duct when the counter-rotating vortices grew to full strength and occupied the entire channel. As the aspect ratio reduces to AR = 1:4, the vortices and the heat transfer enhancements are confined to the leading and trailing surfaces. Murata and Mochizuki [5] studied the heat transfer in a two-pass smooth square channel with sharp 180 deg turns for both the stationary and rotating conditions. They found that in the stationary case, the heat transfer in and after the turn was increased due to flow impingement, flow separation and reattachment, and the reversed flow at the second outer corner. In the rotating case, high-momentum fluid on the upstream pressure side formed one strong vortex in the turn that transported the high-momentum and low-temperature fluid to the suction-surface side, where the heat transfer became high.

Among the experimental studies on this subject, the one conducted by Martin et al. [17] will be used to compare with the numerical simulations conducted in the present study. Through the application of particle image velocimetry (PIV), Martin et al. were able to clearly present the flow characteristics in a U-shaped channel at a Reynolds number range of $109 \leq Re \leq 872$. They found that at $Re \leq 381$, the flow in the bend was time-independent and was stable downstream from the bend. The time-independent nature of the flow in the bend was seen in both the streamwise and crossflow planes. At $Re \geq 436$, however, the flow in the bend was clearly time-dependent in both the streamwise and crossflow planes and was unstable downstream from the bend.

Son et al. [4] also used PIV to study the correlation between high Reynolds number turbulent flow ($Re = 30,000$) and wall heat transfer characteristics in a two-pass square channel with both a smooth wall and a rib-roughened wall. They found that flow impingement was the main factor for heat transfer enhancement in the two-pass square channel. The regions of flow impingement induced by the main flow or secondary flows were well matched with the regions of local heat transfer enhancement. For the smooth-wall cases, there were two pairs of counter-rotating vortices in the secondary flows. A pair of relatively weaker vortices developed inside the flow-separation zone along the separator, and another pair of stronger vortices developed outside the flow-separation zone. These two pairs of vortices tended to merge after the flow was attached to the separator. In addition, the tiny vortices developed at each corner of the cross sectional plane tended to locally decrease the heat transfer.

Using the naphthalene sublimation method, Han et al. [8] studied the detailed mass transfer distributions around sharp 180 deg turns in a two-pass smooth square channel and in an identical channel with two rib-roughened opposite walls. It was found that for the smooth channel, the mass transfer around the turn is influenced by flow separation at the tip of the divider wall and the secondary flow induced by the centrifugal force at the turn. The mass transfer in the turn is also high compared with that before the turn, except at the first outside corner of the turn. For the rib-roughened channel, the mass transfer around the turn is influenced not only by the flow separation and the secondary flow at the turn, but also by the presence of repeated ribs on the top and bottom walls. The mass transfer coefficients on the smooth side walls and on the rib-roughened top and bottom walls around the turn are larger than the corresponding coefficients for the smooth channel.

A review of the previous numerical studies of flow and heat transfer in a two-pass square channel with a 180 deg turn indicated that LES is an effective prediction tool for highly turbulent flows in such a configuration. However, only in-house codes are applied in the previous studies. This paper presents the numerical simulation results for this configuration obtained by LES using FLUENT, a commercial computational fluid dynamics software package. The main goal of the present study is to test whether FLUENT is capable of providing solutions for the flow with the features of the secondary motion and the onset of instabilities.

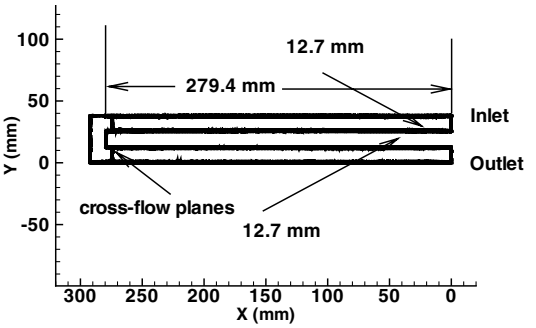

a) Simulation domain

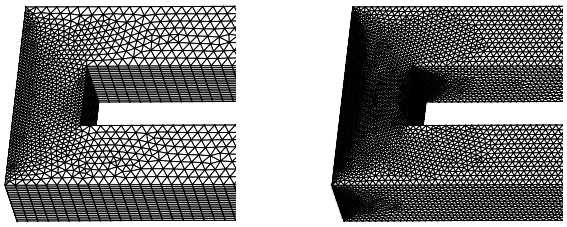

b) Coarse grid at the U-bend **c) Fine grid at the U-bend**

Fig. 1 Simulation domain with example grid.

Simulation Overview

In the following section, the computational grid and domain, numerical method, boundary conditions, and turbulence model are summarized.

Problem Description

The study case was originally posted at the 14th Annual Conference of the Computational Fluid Dynamics Society of Canada (CFD2006) as a challenging exercise. The experimental results were provided by Martin et al. [17] for code validation and performance assessment. The calculation domain is a U-shaped square channel with a 12.7 mm cross section and a gap of 12.7 mm between the inlet and outlet sections. The distance between the start of the flow channel and the beginning of the U-bend was 279.4 mm (see Fig. 1a).

Grid and Numerical Approach

Two mesh schemes (see Figs. 1b and 1c) were generated for the calculations and the grid sensitivity study. The coarse grid (referred to as "G1-O" throughout) consisted of 246,752 cells with a maximum volume of 2.1×10^{-9} m^3, and the finer grid (referred to as "G2-O" throughout) consisted of 524,275 cells with a maximum volume of 6.3×10^{-10} m^3. The mesh scheme G1-O was generated by meshing inner walls and outer walls using regular quadrilateral mesh elements and meshing the top wall and bottom walls using irregular triangular mesh elements. The important advantage of using irregular triangular mesh elements on the top and bottom walls is that the mesh aligned to the sharp corners in the U-bend does not need to be stretched with the wall boundary-layer grid as the structured mesh

Table 1 Grid information: coarse grid (G1-O), coarse grid with refinement (G1-A), finer grid (G2-O), and finer grid with refinement (G2-A)

	$Re = 109$		$Re = 382$		$Re = 872$	
Mesh	Cells	Δy^+	Cells	Δy^+	Cells	Δy^+
G1-O	246,752	1.72	246,752	4.04	——	——
G1-A	340,819	1.02	885,596	1.48	831,750	2.81
G2-O	542,275	1.73	524,275	3.96	524,275	6.96
G2-A	696,776	1.51	1,239,451	1.34	1,025,874	2.97

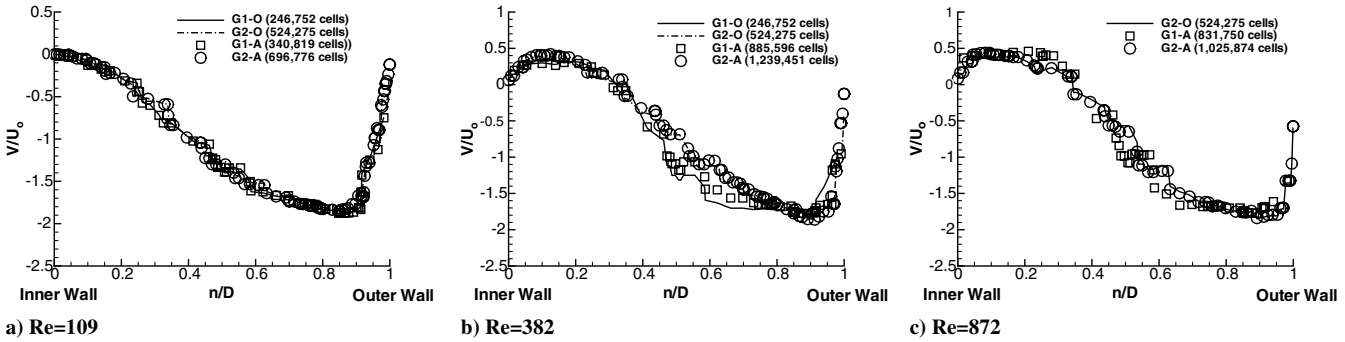

Fig. 2 Grid sensitivity study: mean streamwise velocity comparisons at $z/D = 0.5$ in the center of the U-bend [$n/D = (x - 0.2794)/0.0127$].

does. The mesh scheme G2-O was generated by meshing all faces using irregular triangular mesh elements. For both mesh schemes, the volumes were meshed using tetrahedral elements. It was found that mesh G2-O has a higher quality regarding the mesh skewness. The mesh skewness is assessed using the equiangle skew Q_{EAS} [18], which is a normalized measure of skewness that is defined as follows:

$$Q_{\text{EAS}} = \max\left\{\frac{\theta_{\max} - \theta_{\text{eq}}}{180 - \theta_{\text{eq}}}, \frac{\theta_{\text{eq}} - \theta_{\min}}{\theta_{\text{eq}}}\right\} \tag{1}$$

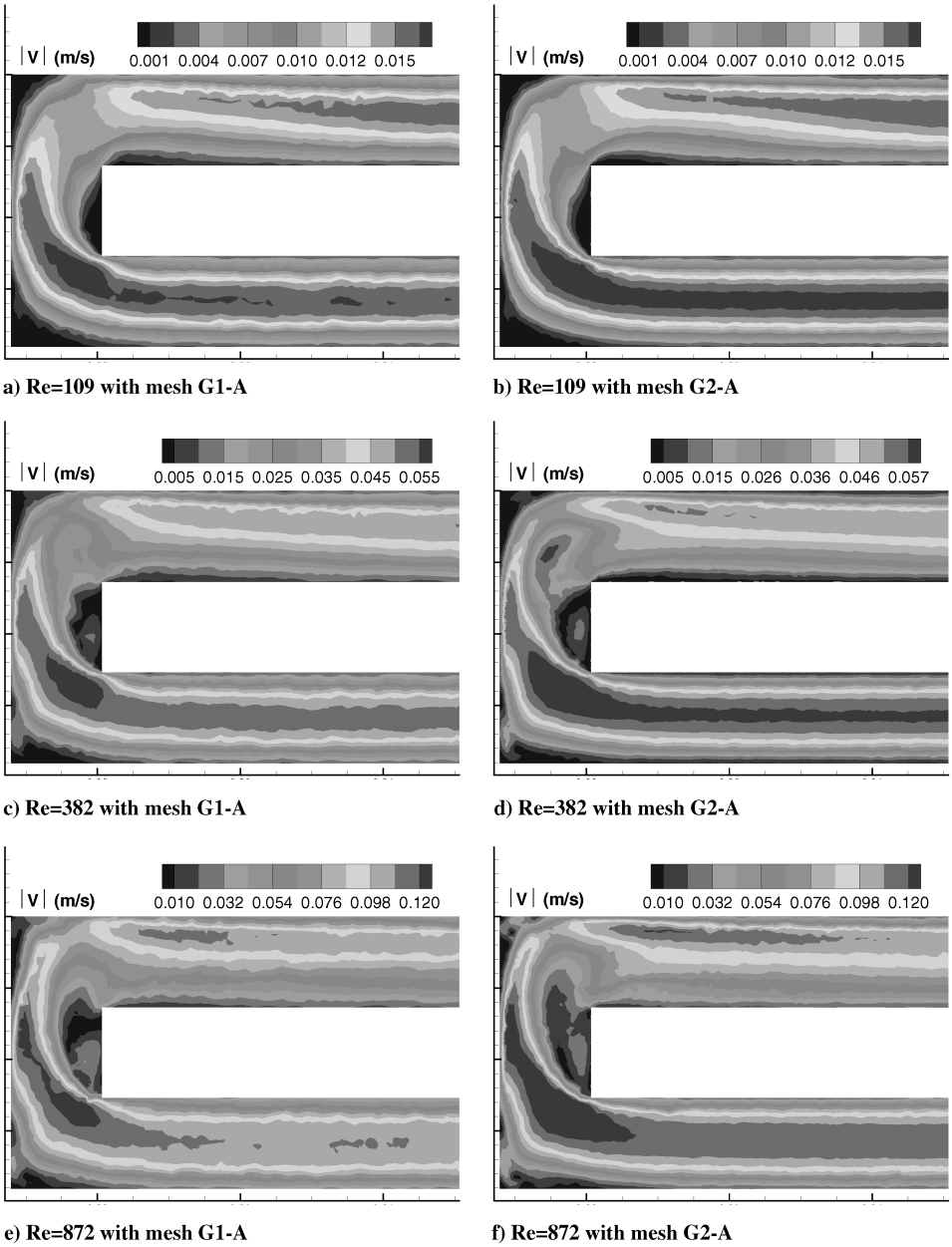

Fig. 3 Grid sensitivity study: mean velocity magnitude comparisons at $z/D = 0.5$.

where θ_{max} and θ_{min} are the maximum and minimum angles (in degrees) between the edges of the element, and θ_{eq} is the characteristic angle corresponding to an equilateral cell of similar form. For triangular and tetrahedral elements, $\theta_{eq} = 60$. By definition, $0 \leq Q_{EAS} \leq 1$, where $Q_{EAS} = 0$ describes an equilateral element, and $Q_{EAS} = 1$ describes a completely degenerate (poorly shaped) element. Both solution-adaptive refinement and boundary-adaptive refinement (features of FLUENT) were used with refinements in the calculation domain, mainly in the U-bend. In G2-O, no cells have an equiangle skew value over 0.75, and 99.8% of cells have equiangle skew values smaller than 0.5. In G1-O, 0.25% cells have equiangle skew values over 0.75, and 3.8% cells have

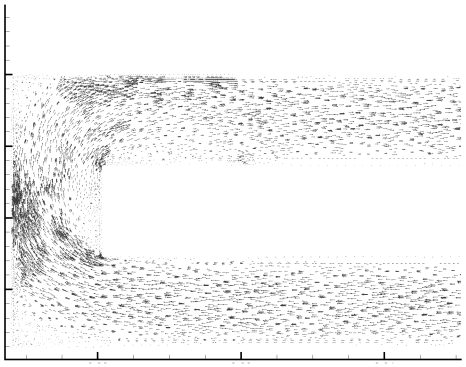

a) Velocity vector field at z/D=0.5

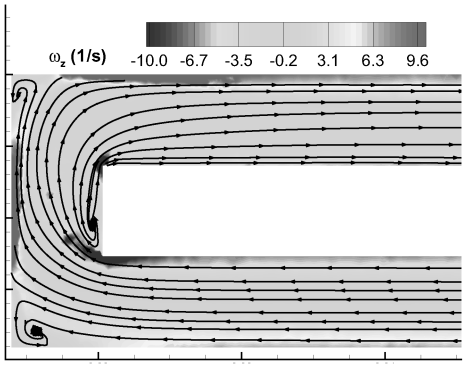

b) Streamlines with out-of-plane vorticity contour at z/D=0.5

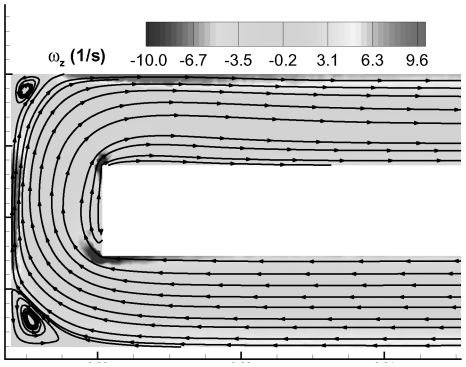

c) Streamlines with out-of-plane vorticity contour at z/D=0.3

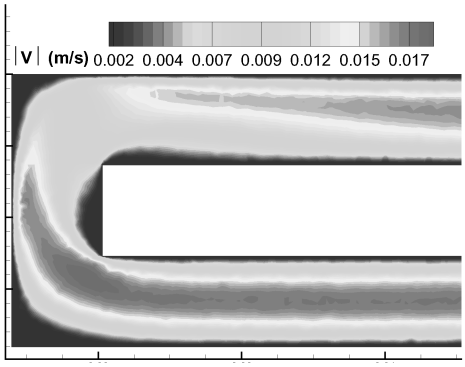

d) Velocity magnitude contour at z/D=0.5

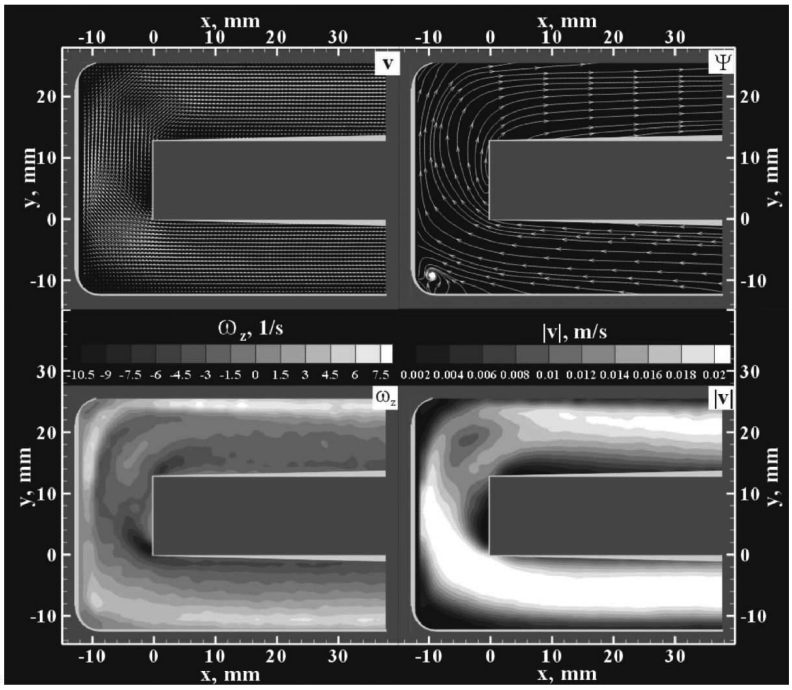

e) PIV results [17] at z/D=0.5. Clockwise from top left: velocity vector field, velocity streamlines, out-of-plane vorticity contours and velocity magnitude

Fig. 4 Comparison of the instantaneous flowfield at $Re = 109$ in streamwise planes.

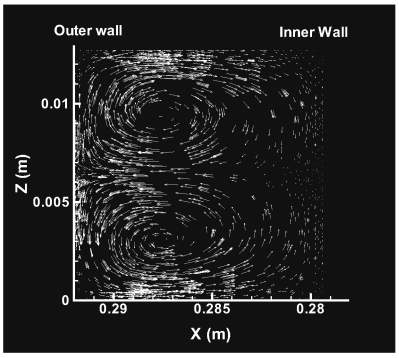

a) Velocity vector field

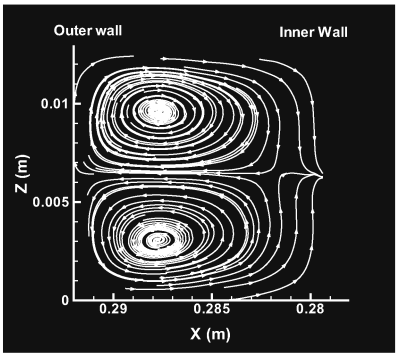

b) Velocity streamlines

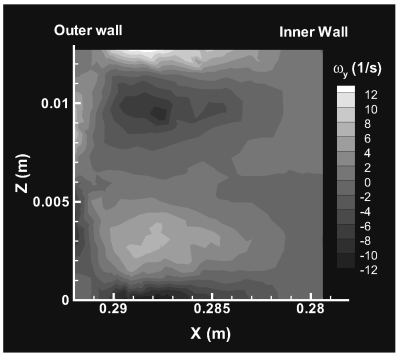

c) Out-of-plane vorticity contours

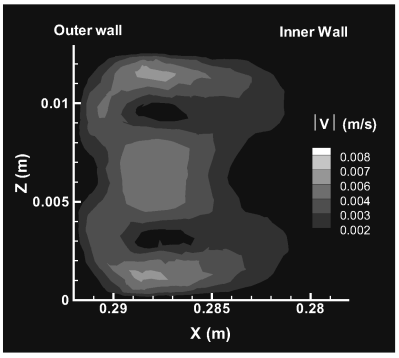

d) Velocity magnitude

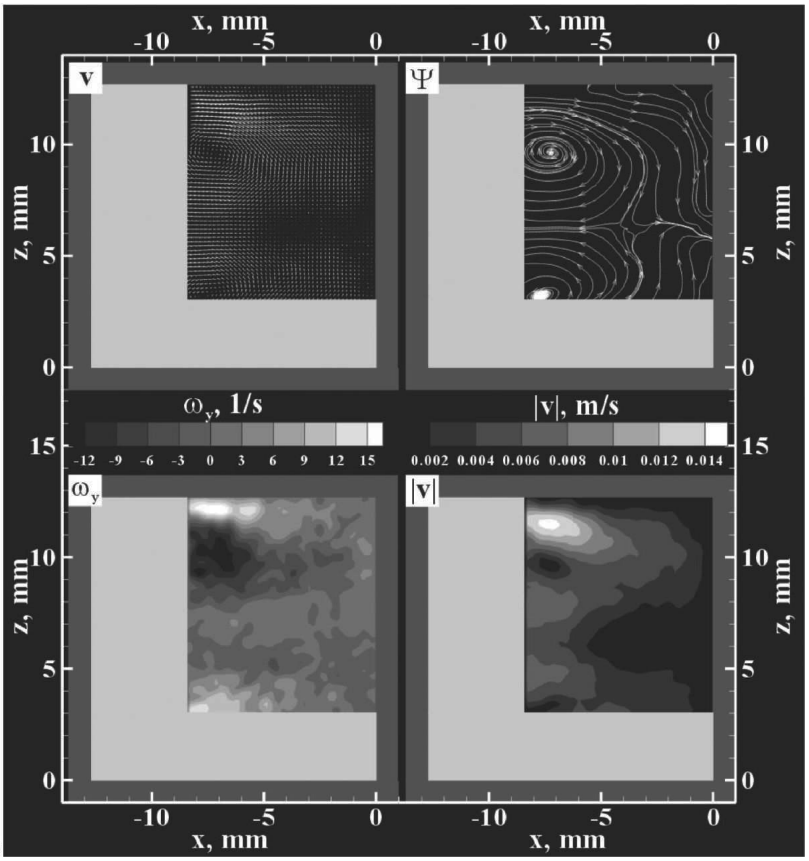

e) PIV results: [17] Clockwise from top left: velocity vector field, velocity streamlines, out-of-plane vorticity contours and velocity magnitude

Fig. 5 Comparison of the instantaneous flowfield at $Re = 109$ in crossflow planes at the center of the bend.

equiangle skew over 0.5. Gradients of velocity magnitude and static pressure have been selected as the field variables for adapting the grid. The number of grid points after refinement for calculations with three different Reynolds numbers is given in Table 1. After refinement, the finest grid consists of 1,239,451 cells. In the final solutions, no Δy^+ values over 3 exist anywhere in the flow domain for the simulation with a Reynolds number of 872, and no Δy^+ values over two exist anywhere in the flow domain for the simulations with Reynolds number of 109 and 382. The results of the grid sensitivity study are plotted in Figs. 2 and 3. Figure 2 shows the mean streamwise velocity at the symmetry plane $z/D = 0.5$ in the center of the U-bend as predicted on different grids for three Reynolds numbers. No such experimental data are available for comparison. It is observed that the results of two coarse-grid sets (G1-O and G1-A) are consistent with those of the finer-grid sets (G2-O and G2-A) for flow with a Reynolds number of 109, but a clear discrepancy can be found between solutions obtained by two grid schemes for $Re = 382$ and 872 (Figs. 2b and 2c). It can also be seen that there is only a moderate change in the results when the mesh resolution is refined for a specific mesh scheme. It is obvious that even with the coarse grid G1-O, the simulations provide realistic results (except for the $Re = 872$ case). For $Re = 872$, G1-O is too coarse to provide a realistic solution. The mean velocity magnitude contours shown in Fig. 3 indicate that the flow features were predicted reasonably well by both mesh schemes, although the low-velocity zone near the top of the U-bend close to the middle of the channel is more pronounced in the G2-A for $Re = 382$. The flow enters the U-bend from right to left through the lower section of the channel and exits from left to right through the upper section. In the rest of this paper, only results from G2-A are presented.

In the present study, a random two-dimensional vortex method proposed by Sergent [19] was adopted for the inlet boundary-condition setup. With this approach, perturbations are added to a specified mean velocity profile via a fluctuating vorticity field (i.e. two-dimensional in the plane normal to the streamwise direction). This vorticity field is generated randomly, but based on the Lagrangian form of the two-dimensional evolution equation of the vorticity and the Biot–Savart law. Ten percent of turbulent intensity and 190 vortices were used in all calculations, because the turbulent intensity conditions for the experimental setup in the PIV test [17] are unknown. The performance of the vortex method was investigated recently and the validations were reported for fully developed turbulent channel flow, pipe flow and separated hill flow [20].

It is shown that the vortex method offers a relatively inexpensive and accurate way to generate random fluctuations representing a turbulent flowfield and the inlet. A pressure-outlet boundary condition was used to define the static pressure at the flow outlet, and it was set to be equal to the operating pressure of 101,325 Pa (default value in FLUENT [21]). For all the calculations, a bounded central-differencing scheme developed by Leonard [22] was used for space discretization, and the second-order implicit scheme was used for time discretization. The standard SIMPLE algorithm was adopted for the velocity-pressure coupling and pressure interpolation. The dynamic Smagorinsky–Lilly subgrid-scale model was used in this study. The nondimensional time step ($t^* = tU_o/D$) for all calculations was between 0.005 and 0.01. The simulations were performed on a SGI Altix 3000 with 64 processors. It needed 20 to 40 s of CPU time for each time step for the coarse grid (246,752 cells) and around 3 min and 40 s of CPU time for each time step for the finest grid (1,239,451 cells). The last 2800 time steps were used to obtain the time-averaged results, and each time step took between 8 and 14 subiterations to converge. In total, about 235 CPU hours were spent for 3800 time steps to complete the simulation with a Reynolds number of 382. Convergence was declared when the maximum scaled residuals were less than 10^{-4} for the continuity and velocity equations.

Large-Eddy Simulation Model

LES, which resolves the large eddies and models the smaller scales, is attractive for massively separated flows because it resolves more flow details than with the conventional approach, in which all the turbulent motions are modeled. The governing equations employed for LES are obtained by filtering the time-dependent Navier–Stokes equations in either Fourier (wave-number) space or configuration (physical) space.

In FLUENT, the finite-volume discretization itself implicitly provides the filtering operation:

$$\bar{\phi}(\mathbf{x}) = \frac{1}{V}\int_{\mathcal{V}} \phi(\mathbf{x}')\,d\mathbf{x}', \qquad \mathbf{x}' \in \mathcal{V} \tag{2}$$

where V is the volume of a computational cell. The filter function $G(x, x')$ implied here is then

$$G(\mathbf{x}, \mathbf{x}') = \begin{cases} 1/V & \mathbf{x}' \in \mathcal{V} \\ 0, & \mathbf{x}' \text{ otherwise} \end{cases} \tag{3}$$

Filtering the incompressible Navier–Stokes equations, one obtains

$$\frac{\partial \rho}{\partial t} + \frac{\partial}{\partial x_i}(\rho \bar{u}_i) = 0 \tag{4}$$

and

$$\frac{\partial}{\partial t}(\rho \bar{u}_i) + \frac{\partial}{\partial x_j}(\rho \bar{u}_i \bar{u}_j) = \frac{\partial}{\partial x_j}\left(\mu \frac{\partial \bar{u}_i}{\partial x_j}\right) - \frac{\partial \bar{p}}{\partial x_i} - \frac{\partial \tau_{ij}}{\partial x_j} \tag{5}$$

where τ_{ij} is the subgrid-scale stress defined by

$$\tau_{ij} \equiv \rho\overline{u_i u_j} - \rho \bar{u}_i \bar{u}_j \tag{6}$$

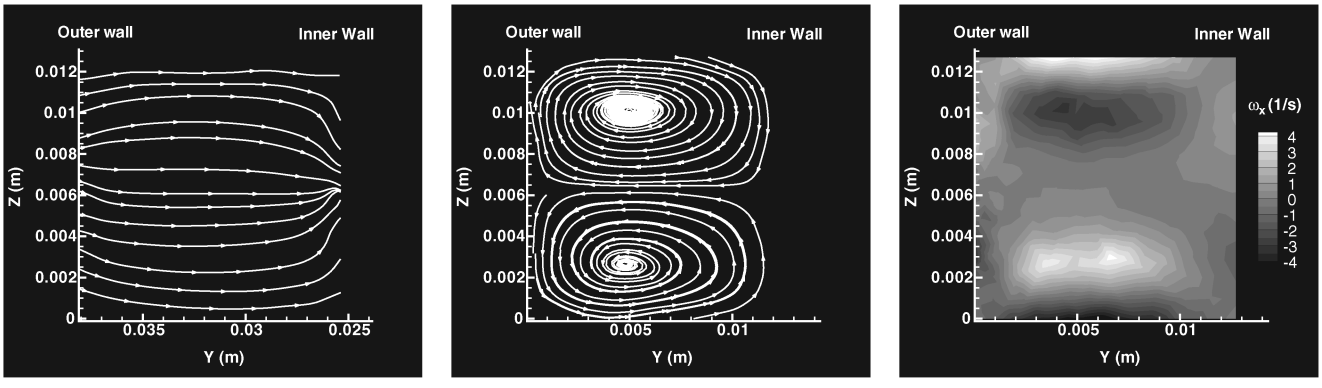

a) Streamline in the first straight passage

b) Streamline in the second straight passage

c) Out-of-plane vorticity contour in the second straight passage

Fig. 6 Instantaneous flowfield in the two straight passages at $x/D = 21.62$ and $Re = 109$.

and modeled by

$$\tau_{ij} - \frac{1}{3}\tau_{kk}\delta_{ij} = -\mu_t\left(\frac{\partial \bar{u}_i}{\partial x_j} + \frac{\partial \bar{u}_j}{\partial x_i}\right) \tag{7}$$

The eddy viscosity μ_t is modeled by [23,24]

$$\mu_t = \rho L_s^2 |\bar{S}| \tag{8}$$

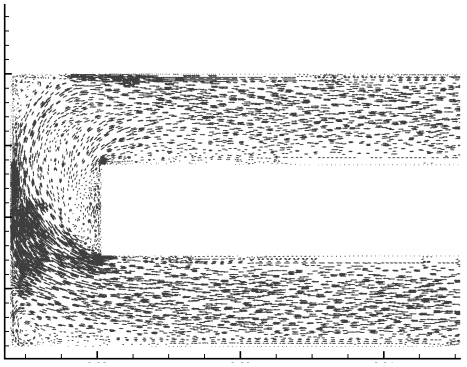

a) Velocity vector field at z/D=0.5

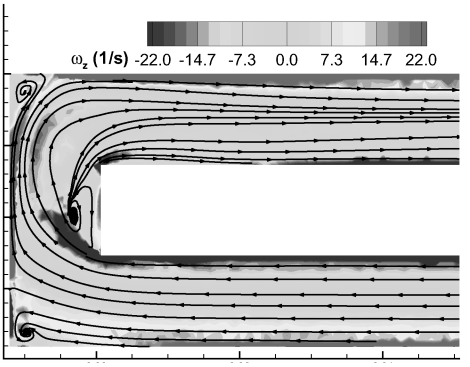

b) Streamlines with out-of-plane vorticity contour at z/D=0.5

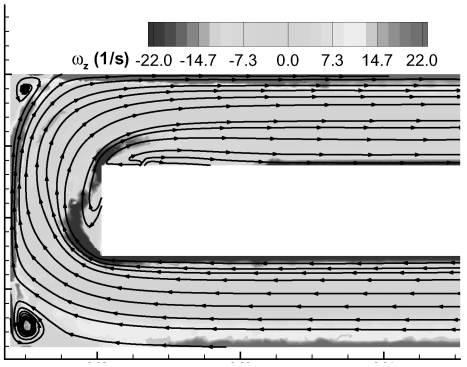

c) Streamlines with out-of-plane vorticity contour at z/D=0.3

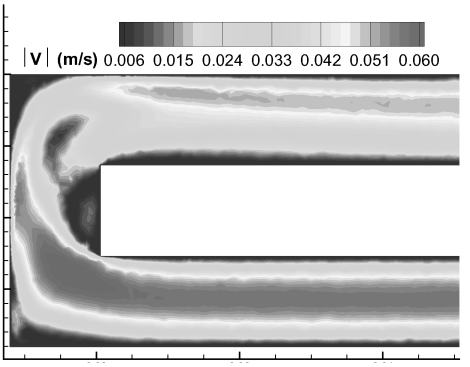

d) Velocity magnitude contour at z/D=0.5

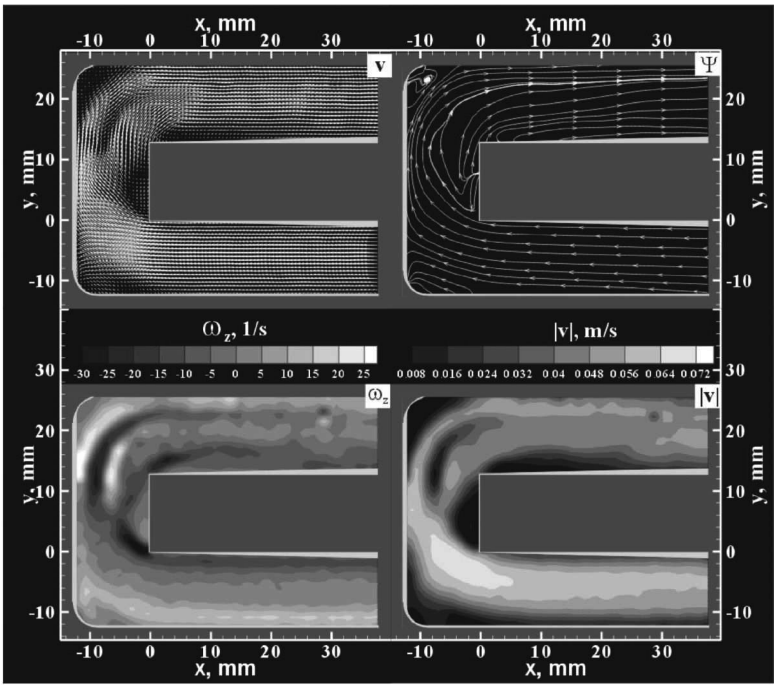

e) PIV results [17] at z/D=0.5. Clockwise from top left: velocity vector field, velocity streamlines, out-of-plane vorticity contours and velocity magnitude

Fig. 7 Comparison of the instantaneous flowfield at $Re = 382$ in streamwise planes.

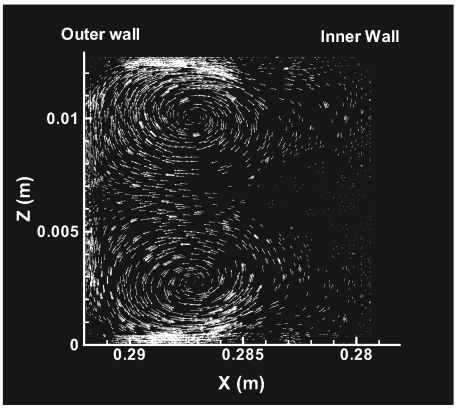

a) Velocity vector field

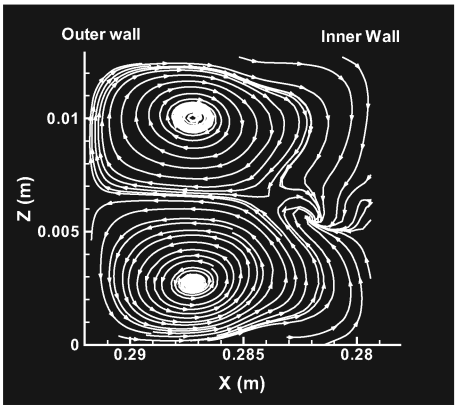

b) Velocity streamlines

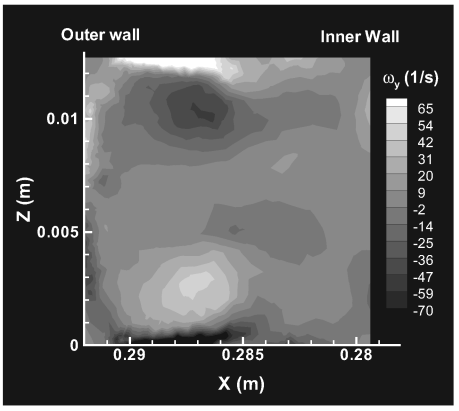

c) Out-of-plane vorticity contours

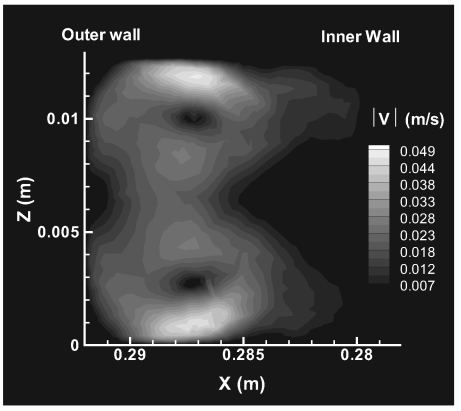

d) Velocity magnitude

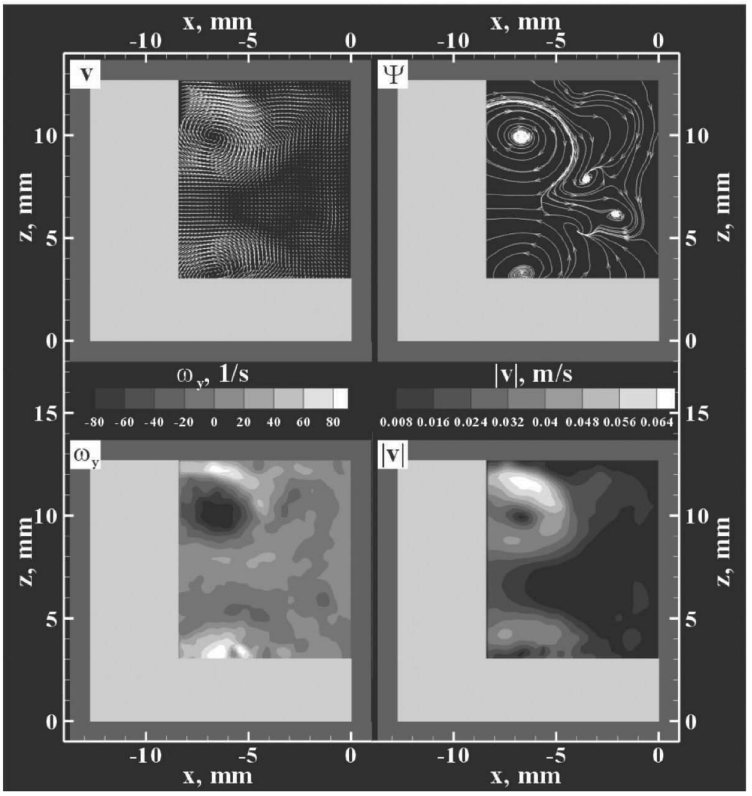

e) PIV results: [17] Clockwise from top left: velocity vector field, velocity streamlines, out-of-plane vorticity contours and velocity magnitude

Fig. 8 Comparison of the instantaneous flowfield at $Re = 382$ in crossflow planes at the center of the bend.

where $|\bar{S}|$ is defined by

$$|\bar{S}| \equiv \sqrt{2\bar{S}_{ij}\bar{S}_{ij}} \tag{9}$$

and $\bar{S}_{ij}$ is defined by

$$\bar{S}_{ij} = \frac{1}{2}\left(\frac{\partial \bar{u}_i}{\partial x_j} + \frac{\partial \bar{u}_j}{\partial x_i}\right) \tag{10}$$

L_s is the mixing length for subgrid scales:

$$L_s = \min(\kappa d, C_s V^{1/3}) \tag{11}$$

where κ is the von Kármán constant, d is the distance to the closest wall, V is the volume of the computational cell, and C_s is the Smagorinsky constant dynamically computed based on the information provided by the resolved scales of motion. The details of the model implementation in FLUENT and its validation can be found in the paper by Kim [25].

Results and Discussion

Various representations of the instantaneous flowfield in the U-bend, as well as in two straight passages, are shown in Figs. 4–13. Distributions of instantaneous flow velocity, out-of-plane vorticity, streamline patterns, and velocity magnitude compared with the PIV results [17] are plotted in both streamwise and crossflow planes in Figs. 4, 5, 7, 8, 10, and 11. The shaded gray regions in images obtained from PIV data represent locations in which no data are available due to optical inaccessibility. In the PIV study, the authors [17] admitted that due to the flow rate uncertainty, the uncertainty in the Reynolds numbers range from 2.5% at the highest flow rate to 20% at the low flow rate. The data presented in their paper [17] were collected at flow rates of 5, 17.5, and 40 lph, which corresponded to Reynolds numbers of 109, 382, and 872, respectively.

Re = 109

Figures 4 and 5 show instantaneous flow patterns at $Re = 109$. The instantaneous images are essentially identical to the time-averaged flow representations (not presented here), which confirms that a steady solution has been obtained for this Reynolds number. This is consistent with the experimental observation of Martin et al. [17]. Furthermore, the characteristic features of the flow captured by the present study are also consistent with those presented in PIV results: two high-vorticity regions associated with the formation of separated shear layers from the sharp convex corners of the U-bend (see Figs. 4b and 4c) and the expected secondary flow pattern with two symmetric circulation zones in the velocity vector plot and streamline plot at the U-bend (see Figs. 5a and 5b).

In Figs. 5, 8, and 11, the primary flow through the channel is directed toward the reader. The plots of vorticity contour and velocity magnitude contour provide additional descriptions of the circulation-zone structure. The streamlines at two straight passages at $x/D = 19.50$ are plotted in Fig. 6. There are no experimental data available for comparison. In the U-bend, due to the centrifugal forces, the flow moves away from the inner wall to the outer wall. Most likely because of that, as mass compensation, it has been found that flow moves away from the outer wall to the inner wall just before the flow enters the U-bend (Fig. 6a). Instantaneous flowfields in the second straight passage are plotted in Figs. 6b and 6c. It is interesting to find that the secondary flow patterns exhibit the same symmetric recirculation zones as seen in the U-bend (see Fig. 5b), but with a near 30% drop in the maximum magnitude of the vorticity in the contour plot.

Re = 382

Figures 7 and 8 show instantaneous flow patterns at $Re = 382$. The characteristic flow structures that were detected at $Re = 109$ are still present at $Re = 381$. A low-velocity zone is captured near the second inner corner close to the middle of the channel. This is a characteristic feature of the flow in the low Reynolds number regime. The images of streamlines at $z/D = 0.3$ and 0.5 (see Figs. 7b and 7c) show that as the flow approaches the bend, it separates at the outer corners. In the U-bend, along the inner wall, the flow accelerates and separates as it encounters the sharp inner corner toward the center of the channel. The separation is almost sustained through the height of the channel, but the strength of the recirculation is much smaller in the lower plane. In the second straight passage, another recirculation region along the inner wall is also detected (see Fig. 7c). This flow feature is consistent with the simulation results obtained by Viswanathan and Tafti [16] using a DES model for a ribbed channel with 12 ribs in the first and second passages for a Reynolds number of 20,000. Their calculations were carried out with a uniform laminar flow inlet profile.

In the cross-stream plane (Fig. 8), the secondary flow patterns exhibit the same symmetric secondary recirculation zones as seen at $Re = 109$. However, from the out-of-plane vorticity contour plot (Fig. 8c), it can be seen that the Dean vortices have significantly higher values of circulation. The streamline plot reveals an additional small-scale circulation zone that is induced by the stronger Dean vortex pair. Some discrepancies of the numerical predictions and experimental results can be seen in Figs. 7 and 8. In the cross-stream plane, the predicted velocity magnitude in the present study is about 20% lower than in the experimental data. However, this could be due to the combined effect of the grid resolution, the inlet velocity profile, and the experimental uncertainties. The other discrepancies are that the experimental images reveal extra small-scale circulation zones in the crossflow plane, whereas the simulation plots reveal a stronger recirculation zone in the U-bend in the streamwise plane.

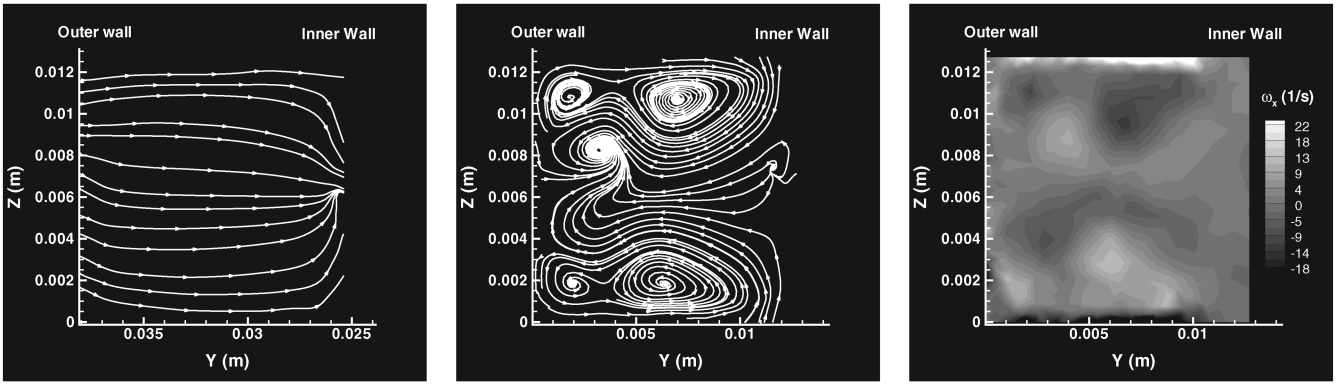

a) Streamline in the first straight passage **b) Streamline in the second straight passage** **c) Out-of-plane vorticity contour in the second straight passage**

Fig. 9 Instantaneous flowfield in the two straight passages at $x/D = 21.62$ and $Re = 382$.

The streamlines at two straight passages at $x/D = 21.62$ are plotted in Fig. 9. The streamline exhibits the same flow pattern seen in the flow with a Reynolds number of 109 in the first straight passage. However, in the second straight passage, the large-scale Dean vortex pair is replaced by a six-cell secondary flow pattern. The presence of the small-scale vortical structures is obvious from both the streamline plot and the out-of-plane vorticity contour.

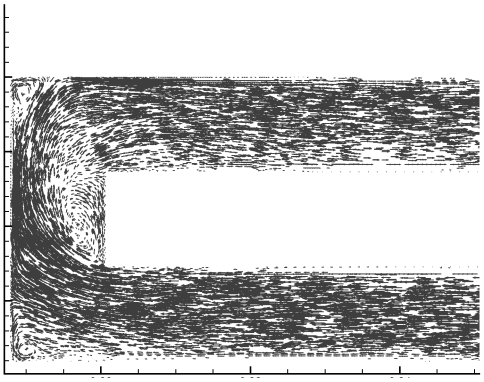

a) Velocity vector field at z/D=0.5

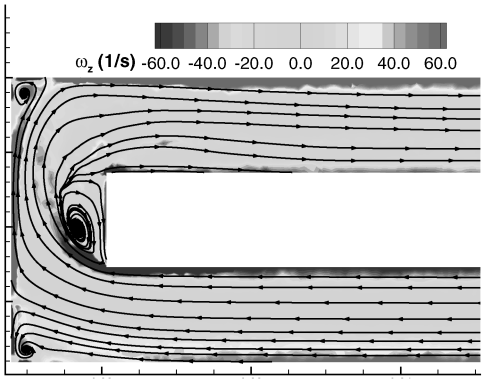

b) Streamlines without-of-plane vorticity contour at z/D=0.5

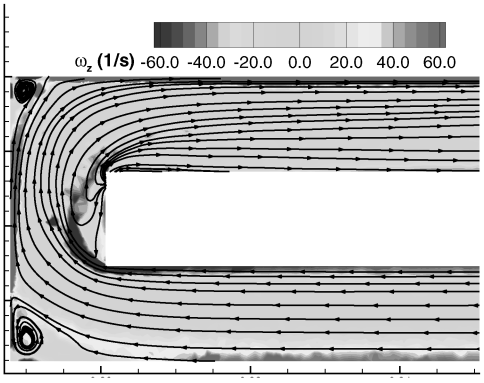

c) Streamlines with out-of-plane vorticity contour at z/D=0.3

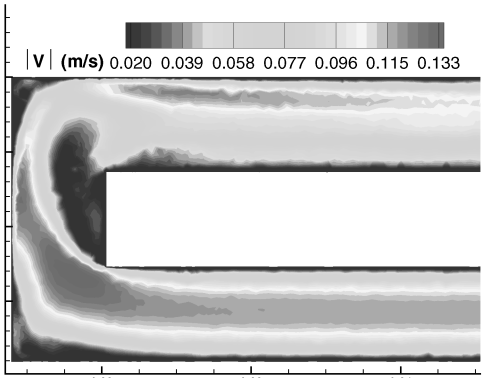

d) Velocity magnitude contour at z/D=0.5

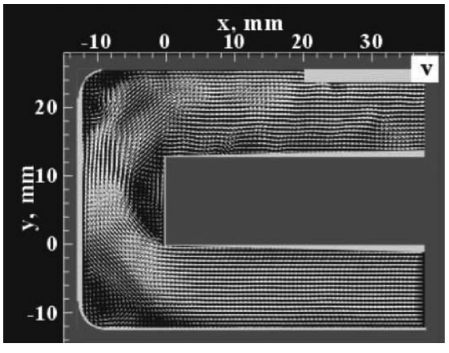

e) PIV results [17] at z/D=0.5: velocity vector field

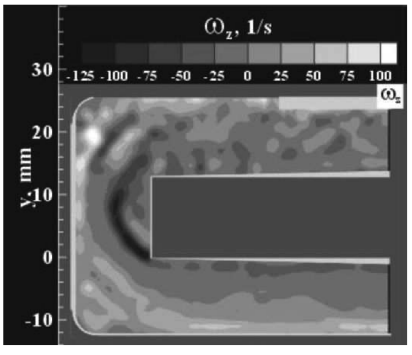

f) PIV results [17] at z/D=0.5: out-of-plane vorticity contour

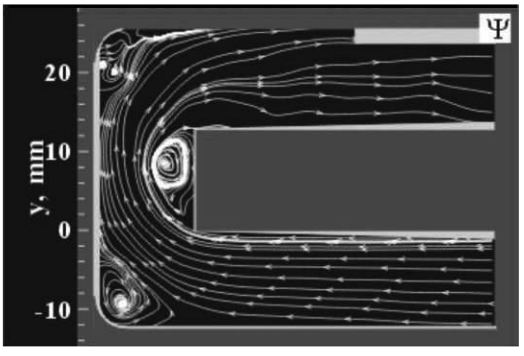

g) PIV results [17] at z/D=0.5: velocity streamlines

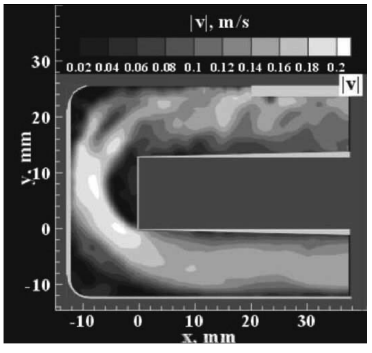

h) PIV results [17] at z/D=0.5: velocity magnitude contour

Fig. 10 Comparison of the instantaneous flowfield at $Re = 872$ in streamwise planes.

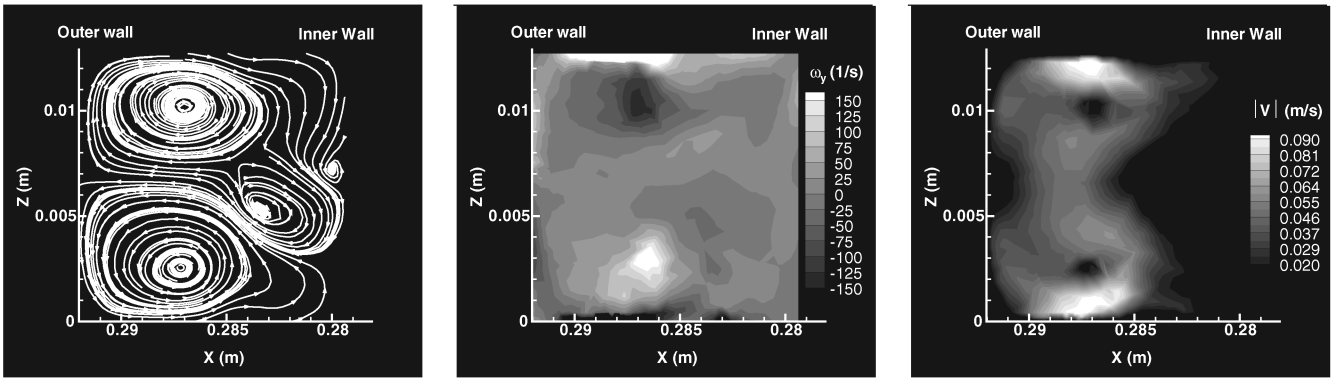

a) Velocity streamlines b) Out-of-plane vorticity contour c) Velocity magnitude contour

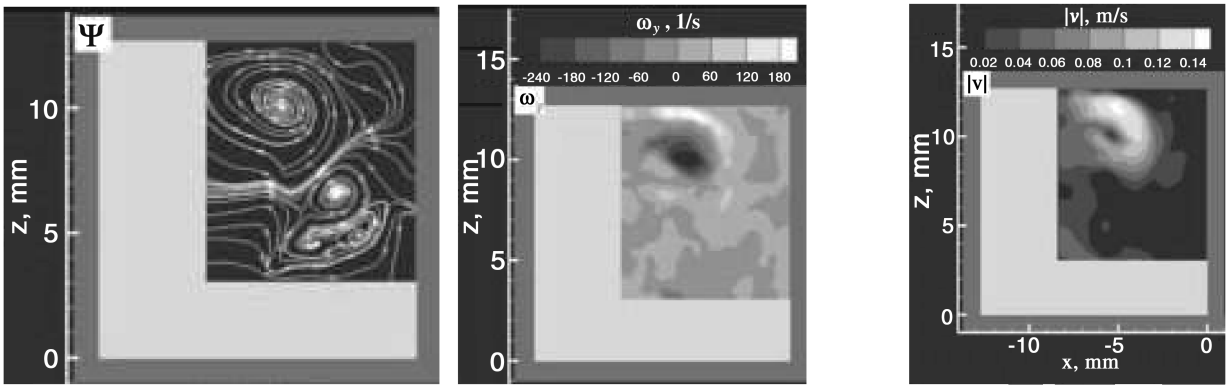

d) PIV results [17]: velocity streamlines e) PIV results [17]: out-of-plane vorticity contour f) PIV results [17]: velocity magnitude contour

Fig. 11 Comparison of the instantaneous flowfield at $Re = 872$ in crossflow planes at the center of the bend.

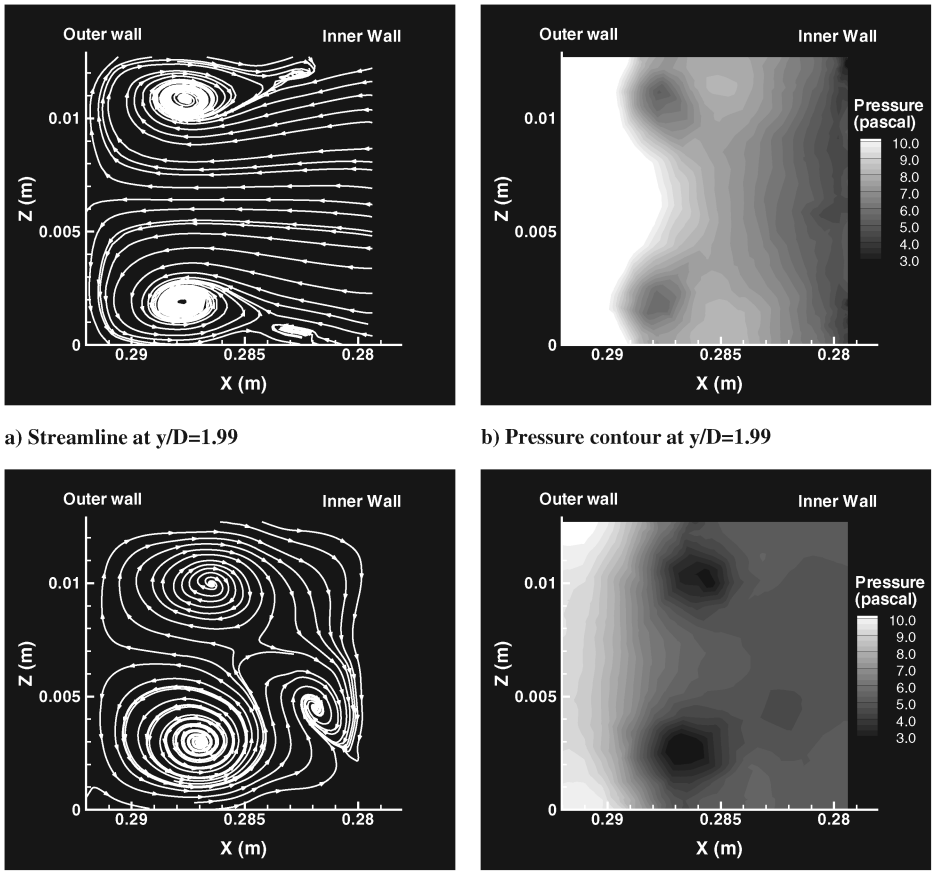

a) Streamline at y/D=1.99 b) Pressure contour at y/D=1.99

c) Streamline at y/D=1.33 d) Pressure contour at y/D=1.33

Fig. 12 Instantaneous flowfield at $Re = 872$ in crossflow planes in the U-bend.

***Re* = 872**

The instantaneous flowfield at a Reynolds number of 872 in the streamwise plane is plotted in Fig. 10. Comparison of Fig. 10b with Fig. 10g shows good agreement between the present simulation results and the previous experimental data [17]. In both studies, three recirculating zones have been clearly observed in the streamline plots. It should be noted that for a lower Reynolds number, the shear layer that forms at the first inner corner of the U-bend reattaches to the vertical portion of the inner wall before or close to the second inner corner (see Fig. 4b). In both Figs. 10b and 10g, it is obvious that the flow remains separated from the inner wall past the second corner of the U-bend. Comparison of the instantaneous flowfield at $Re = 872$ in crossflow planes at the center of the bend is plotted in Fig. 11. Furthermore, the streamlines and static pressure contours at two additional locations in the bend are plotted in Fig. 12. It is obvious that the large-scale Dean vortex pair, the feature of the secondary flow in curved pipes or channels, remains dominant in all locations. The centers of these vortices are strongly associated with the

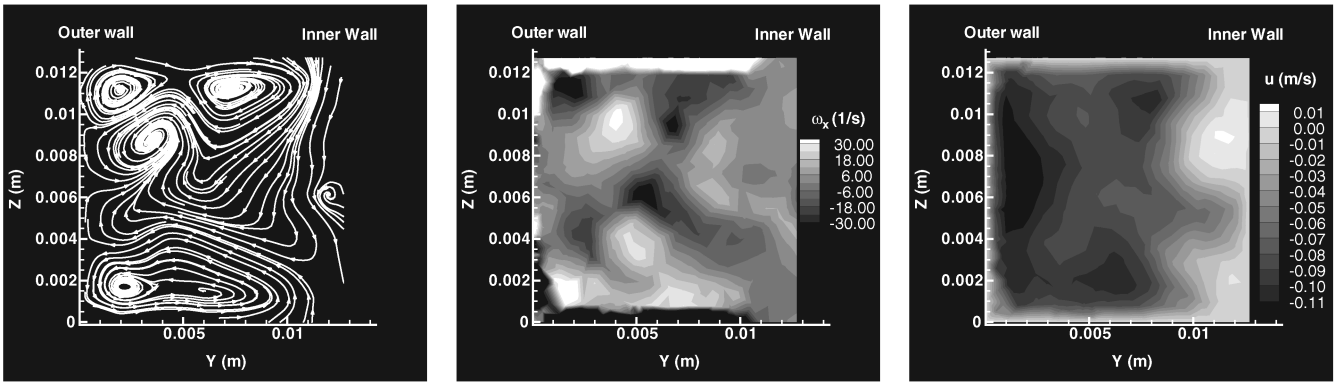

a) Streamline b) Out-of-plane vorticity contour c) Streamwise velocity contour

Fig. 13 Instantaneous flowfield at $Re = 872$ in the second straight passages at $x/D = 21.62$.

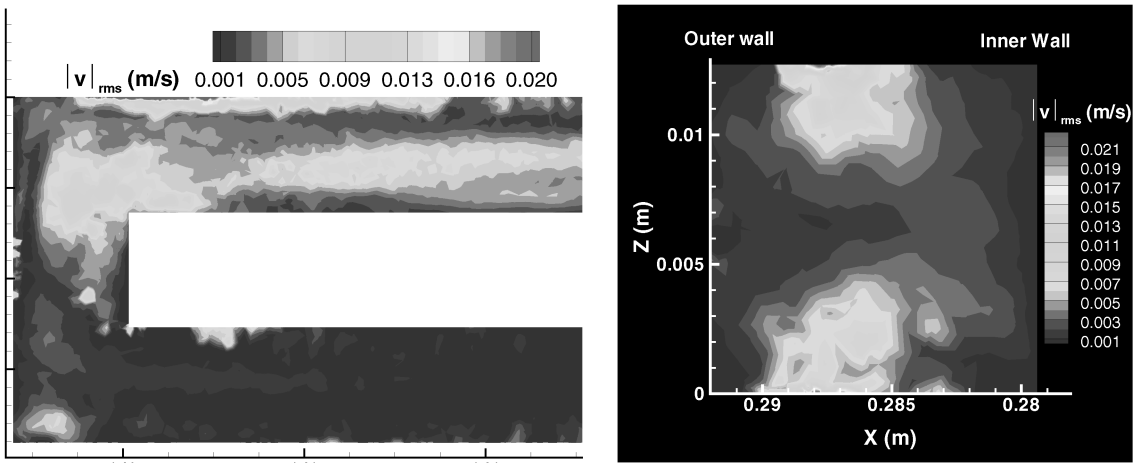

a) Streamwise plane at z/D=0.5 b) Cross-flow plane at the center of the bend

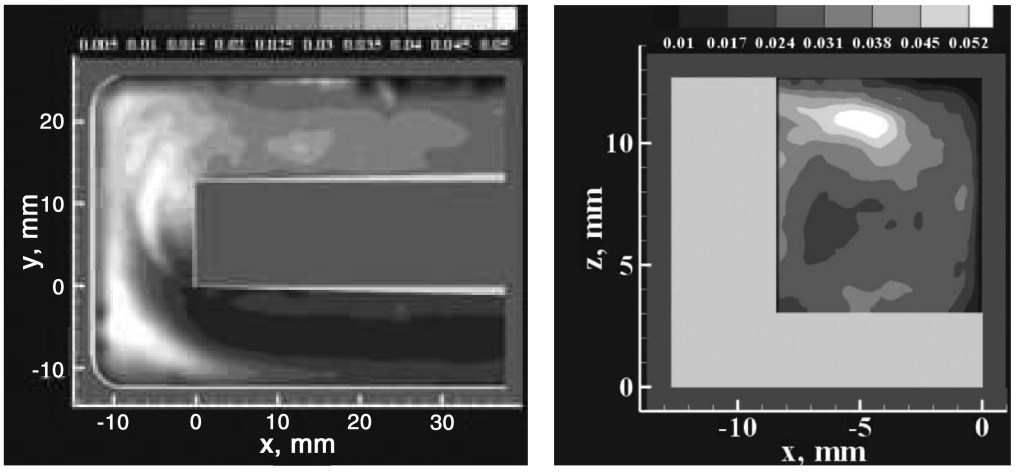

c) Streamwise plane at z/D=0.5 d) Cross-flow plane at the center of the bend

Fig. 14 Comparison of root-mean-square velocity fluctuations at $Re = 872$: a)–b) present simulation and c)–d) PIV results [17].

lower-pressure centers. This confirms that the secondary flow can be attributed principally to the effect of the centrifugal pressure gradient in the main flow acting on the relatively stagnant fluid in the wall boundary layer. The Dean vortex pair exhibits a symmetric structure in the U-bend.

A previous experimental study [17] found that the distinguishing feature of the secondary flow at this high-flow-rate regime is the presence of the small-scale vortices that are induced by the stronger fluctuating Dean vortex pair. These small-scale vortices are captured in the present study (see Figs. 11 and 12). The instantaneous flowfield in the second straight passage at $x/D = 21.62$ is plotted in Fig. 13. The flow pattern exhibits similarity, as seen at $Re = 382$ (see Figs. 9b and 9c). There is a zone with positive streamwise velocity along the inner wall, which shows that flow separation occurred. Unsymmetrical small-scale vortices become a dominant feature of the secondary flow in the second straight passage, instead of the large-scale Dean vortex pair observed at $Re = 109$. Although comparison of the present results with previous experimental data showed that the prediction successfully reproduced most of the flow features associated with the secondary motion, some discrepancies of the numerical prediction and experimental results are obvious. The present simulation underpredicts velocity magnitude in both the streamwise (Fig. 10) and crossflow planes (Fig. 11). It also underpredicts the flow unsteadiness, which is indicated by a lower value in root-mean-square velocity fluctuation contours (see Fig. 14).

Conclusions

The LES model in FLUENT was used to predict the flow through a U-shaped channel with a square cross section at Reynolds numbers of 109, 382, and 872. Despite the fact that the grids used were relatively coarse for LES at Reynolds numbers of 382 and 872 and the experimental information about the inlet velocity profiles was limited, the agreement between the predictions and corresponding experimental data was generally satisfactory. Some of the main observations and conclusions are summarized:

1) At $Re = 109$, a steady flow solution was obtained and that is consistent with the experimental observation [17].

2) Consistent with the PIV results [17] at the midpoint of the turn, the secondary flow pattern with two symmetric circulation zones (Dean vortices) is observed at $Re = 109$. Extra small-scale circulation zones that are induced by the stronger Dean vortex pair are observed with an increase of the Reynolds number.

3) In the second straight passage, two symmetric circulation zones are present at $Re = 109$. At $Re = 382$ and 872, the unsymmetrical small-scale vortices become a dominant feature of the secondary flow.

4) A characteristic feature of the flow in a low Reynolds number regime is captured in the present simulations: a low-velocity zone is present in the flowfield close to the middle of the channel near the second inner corner.

5) A few other characteristic flow structures at the U-bend are also captured in the present simulations. Two recirculating zones at the outer corners are present along with one near the inner wall. Also, two high-vorticity regions along the inner wall of the U-bend are associated with the formation of separated shear layers from the sharp corners.

6) The present results underpredict the velocity field and the flow unsteadiness, especially at higher Reynolds number.

7) Discrepancies between the predictions and the experimental data are thought to be due to the combined effect of the grid resolution, the inlet velocity profile, and the experiment uncertainties (especially at lower Reynolds number).

In summary, it is very encouraging that the numerical simulation results are comparable with the measurements using PIV. In this work, numerical solutions provided a clear picture of the secondary motion in the U-bend as well as in the second straight passage, which can help us to better understand flow characteristics. The present study gave confidence in the numerical simulations of flow through curved square ducts or serpentine channels.

Acknowledgments

Computing infrastructure for this work was provided by grants from the Canada Foundation for Innovation, British Columbia Knowledge Development Fund, SGI Canada, and donors to the University of Northern British Columbia (project 8834).

References

[1] Ekkad, S. V., and Han, J.-C., "Detailed Heat Transfer Distributions in Two-Pass Square Channels with Rib Turbulators," *International Journal of Heat and Mass Transfer*, Vol. 40, No. 11, 1997, pp. 2525–2537. doi:10.1016/S0017-9310(96)00318-3

[2] Park, C. W., Kandis, M., and Lau, S. C., "Heat/Mass Transfer Distribution in a Rotating Two-Pass Square Channel," *International Journal of Rotating Machinery*, Vol. 4, No. 3, 1998, pp. 175–188. doi:10.1155/S1023621X98000153

[3] Liou, T.-M., Tzeng, Y.-Y., and Chen, C.-C., "Fluid Flow in a 180 Deg Sharp Turning Duct with Different Divider Thicknesses," *Journal of Turbomachinery*, Vol. 121, No. 3, 1999, pp. 569–576.

[4] Son, S. Y., Kihm, K. D., and Han, J.-C., "PIV Flow Measurements for Heat Transfer Characterization in Two-Pass Square Channels with Smooth and 90 Deg Ribbed Walls," *International Journal of Heat and Mass Transfer*, Vol. 45, No. 24, 2002, pp. 4809–4822. doi:10.1016/S0017-9310(02)00192-8

[5] Murata, A., and Mochizuki, S., "Large Eddy Simulation of Turbulent Heat Transfer in a Rotating Two-Pass Smooth Square Channel with Sharp 180 Deg Turns," *International Journal of Heat and Mass Transfer*, Vol. 47, No. 4, 2004, pp. 683–698. doi:10.1016/j.ijheatmasstransfer.2003.07.022

[6] Sewall, E. A., Tafti, D. K., Graham, A. B., and Thole, K. A., "Experimental Validation of Large Eddy Simulations of Flow and Heat Transfer in a Stationary Ribbed Duct," *International Journal of Heat and Fluid Flow*, Vol. 27, No. 2, 2006, pp. 243–258. doi:10.1016/j.ijheatfluidflow.2005.08.010

[7] Metzger, D. E., Plevich, C. W., and Fan, C. S., "Pressure Loss Through Sharp 180 Deg Turns in Smooth Rectangular Channels," *Journal of Engineering for Gas Turbines and Power*, Vol. 106, No. 3, 1984, pp. 677–681.

[8] Han, J. C., Chandra, P. R., and Lau, S. C., "Local Heat/Mass Transfer Distributions Around Sharp 180 Deg Turns in Two-Pass Smooth and Rib-Roughened Channels," *Journal of Heat Transfer*, Vol. 110, No. 1, 1988, pp. 91–98.

[9] Metzger, D. E., and Sahm, M. K., "Heat Transfer Around Sharp 180 Deg Turns in Smooth Rectangular Channels," *Journal of Heat Transfer*, Vol. 108, No. 3, 1986, pp. 500–506.

[10] Su, G., Chen, H.-C., Han, J.-C., and Heidmann, J. D., "Computation of Flow and Heat Transfer in Rotating Two-Pass Rectangular Channels (AR = 1:1, 1:2, and 1:4) with Smooth Walls by a Reynolds Stress Turbulence Model," *International Journal of Heat and Mass Transfer*, Vol. 47, No. 26, 2004, pp. 5665–5683. doi:10.1016/j.ijheatmasstransfer.2004.07.019

[11] Chou, J. M., and Anand, N. K., "Heat Transfer in a Serpentine Channel with a Series of Right-Angle Turns," *Numerical Heat Transfer, Part A, Applications*, Vol. 23, No. 2, 1993, pp. 189–210. doi:10.1080/10407789308913668

[12] Mochizuki, S., Murata, A., Shibata, R., and Yang, W.-J., "Detailed Measurements of Local Heat Transfer Coefficients in Turbulent Flow Through Smooth and Rib-Roughened Serpentine Passages with a 180 Deg Sharp Bend," *International Journal of Heat and Mass Transfer*, Vol. 42, No. 11, 1999, pp. 1925–1934.

[13] Chintada, S., Ko, K.-H., and Anand, N. K., "Heat Transfer in 3-D Serpentine Channels with Right-Angle Turns," *Numerical Heat Transfer, Part A, Applications*, Vol. 36, No. 8, 1999, pp. 781–806. doi:10.1080/104077899274453

[14] Syuhada, A., Hirota, M., Fujita, H., Araki, S., Yanagida, M., and Tanaka, T., "Heat (Mass) Transfer in Serpentine Flow Passage with Rectangular Cross Section," *Energy Conversion and Management*, Vol. 42, No. 15, 2001, pp. 1867–1885. doi:10.1016/S0196-8904(01)00047-4

[15] Sewall, E. A., and Tafti, D. K., "Large Eddy Simulations of Flow and Heat Transfer in the 180-Deg Bend Region of a Stationary Gas Turbine Blade Internal Cooling Duct," *Journal of Turbomachinery*, Vol. 128, No. 4, 2006, pp. 763–771. doi:10.1115/1.2098769

[16] Viswanathan, A. K., and Tafti, D. K., "A Comparative Study of DES and URANS for Flow Prediction in a Two-Pass Internal Cooling Duct," *Journal of Fluids Engineering*, Vol. 128, No. 6, 2006, pp. 1336–1345. doi:10.1115/1.2353279

[17] Martin, J., Oshkai, P., and Djilali, N., "Flow Structures in a U-Shaped Fuel Cell Flow Channel: Quantitative Visualization Using Particle Image Velocimetry," *Journal of Fuel Cell Science and Technology*, Vol. 2, No. 1, 2005, pp. 70–80. doi:10.1115/1.1843121

[18] GAMBIT, Software Package, Ver. 2.2, Fluent, Inc., Lebanon, PA, Dec. 2004.

[19] Sergent, E., "Vers une Methodologie de Couplage Entre la Simulation des Grandes Echelles et les Modeles Statistiques," Ph.D. Thesis, L'Ecole Centrale de Lyon, Lyon, France, 2002.

[20] Mathey, F., Cokjat, D., Bertoglio, J. P., and Sergent, E., "Assessment of the Vortex Method for Large Eddy Simulation Inlet Conditions," *Progress in Computational Fluid Dynamics*, Vol. 6, Nos. 1–3, 2006, pp. 58–67. doi:10.1504/PCFD.2006.009483

[21] FLUENT, Software Package, Ver. 6.2, Fluent, Inc., Lebanon, PA, Feb. 2005.

[22] Leonard, B. P., "The Ultimate Conservative Difference Scheme Applied to Unsteady One-Dimensional Advection," *Computer Methods in Applied Mechanics and Engineering*, Vol. 88, No. 1, 1991, pp. 17–74. doi:10.1016/0045-7825(91)90232-U

[23] Smagorinsky, J., "General Circulation Experiments with the Primitive Equations, 1: The Basic Experiment," *Monthly Weather Review* Vol. 91, No. 3, 1963, pp. 99–164. doi:10.1175/1520-0493(1963)091<0099:GCEWTP>2.3.CO;2

[24] Lilly, D. K., "On the Application of the Eddy Viscosity Concept in the Inertial Subrange of Turbulence," National Center for Atmospheric Research Manuscript No. 123, Boulder, CO, 1966.

[25] Kim, S.-E., "Large Eddy Simulation Using Unstructured Meshes and Dynamic Subgrid-Scale Turbulence Models," 34th AIAA Fluid Dynamics Conference and Exhibit, AIAA Paper 2004-2548, June 2004.